ROYAL SOCIETY OF CHEMISTRY

PAPER

Check for updates

Radioactive hybrid semiconducting polymer nanoparticles for imaging-guided tri-modal therapy of breast cancer†

Junhao Gu,‡[a] Danling Cheng,‡[a] Haiyan Li,‡[b] Tao Yu,[a] Zhenghe Zhang,[a] Yue Liu,[a] Xiaoying Wang,*[c] Xia Lu*[b] and Jingchao Li ⓘ *[a]

Due to the rapid progression and aggressive metastasis of breast cancer, its diagnosis and treatment remain a great challenge. The simultaneous inhibition of tumor growth and metastasis is necessary for breast cancer to obtain ideal therapeutic outcomes. We herein report the development of radioactive hybrid semiconducting polymer nanoparticles (SPN_H) for imaging-guided tri-modal therapy of breast cancer. Two semiconducting polymers are used to form SPN_H with a diameter of around 60 nm *via* nano-coprecipitation and they are also labeled with iodine-131 (^{131}I) to enhance the imaging functions. The formed SPN_H show good radiolabeling stability and excellent photodynamic and photothermal effects under 808 nm laser irradiation to produce singlet oxygen ($^1O_2$) and heat. Moreover, SPN_H can generate $^1O_2$ with ultrasound irradiation *via* their sonodynamic properties. After intravenous tail vein injection, SPN_H can effectively accumulate in the subcutaneous 4T1 tumors of living mice as verified *via* fluorescence and single photon emission computed tomography (SPECT) imaging. With the irradiation of tumors using an 808 nm laser and US, SPN_H mediate photodynamic therapy (PDT), photothermal therapy (PTT) and sonodynamic therapy (SDT) to kill tumor cells. Such a tri-modal therapy leads to an improved efficacy in inhibiting tumor growth and suppressing tumor metastasis compared to the sole SDT and combinational PDT–PTT. This study thus demonstrates the applications of SPN_H to diagnose tumors and combine different therapies for effective breast cancer treatment.

Introduction

Breast cancer is a malignant tumor that has seriously affected the survival rate of female patients.[1,2] For decades, the traditional treatment methods including surgery, radiotherapy,[3,4] chemotherapy[5] and their combined therapy have failed to achieve ideal therapeutic outcomes. Surgical excision is the major option for breast cancer, but it may cause the issue of incomplete resection, leading to tumor recurrence.[6,7] Although chemotherapy and radiotherapy can improve the therapeutic effect to a certain extent, there are some inevitable problems such as poor tumor specificity and serious side effects.[8,9] Accordingly, it is important to explore some more effective and safe therapeutic strategies for breast cancer treatment.[10–14]

Jingchao Li received his PhD degree in Materials Science and Engineering from the University of Tsukuba (Japan) in 2017. He then worked as a postdoctoral research fellow in the School of Chemical and Biomedical Engineering, Nanyang Technological University. He is currently a Professor in the College of Biological Science and Medical Engineering at Donghua University. Dr Li has published more than 150 SCI papers in famous international journals such as Nat. Commun., Adv. Mater. and Angew. Chem., Int. Ed. with an H-index of 60. His research focuses on the development of advanced nanomaterials for cancer theranostics.

Jingchao Li

[a] State Key Laboratory for Modification of Chemical Fibers and Polymer Materials, Shanghai Engineering Research Center of Nano-Biomaterials and Regenerative Medicine, College of Biological Science and Medical Engineering, Donghua University, Shanghai 201620, P. R. China. E-mail: jcli@dhu.edu.cn

[b] Department of Nuclear Medicine, Northern Jiangsu People's Hospital, Clinical Medical College, Yangzhou University, Yangzhou 225001, P. R. China. E-mail: lxgf2222@163.com

[c] Office of Hospital Infection and Disease Control and Prevention, Shanghai General Hospital, Shanghai Jiao Tong University School of Medicine, Shanghai 200080, P. R. China. E-mail: goodwxyz@163.com

† Electronic supplementary information (ESI) available. See DOI: https://doi.org/10.1039/d4tb00834k

‡ These authors contributed equally to this work.

This journal is © The Royal Society of Chemistry 2024

J. Mater. Chem. B, 2024, **12**, 6091–6101 | **6091**

In recent years, some therapeutic strategies have shown promising opportunities for cancer treatment, such as photothermal therapy (PTT), photodynamic therapy (PDT) and sonodynamic therapy (SDT).[15] PTT has shown promise as an approach for cancer treatment because the photothermal agents can absorb the optical energy and convert the photoenergy into heat to ablate cancer cells.[16,17] PDT usually utilizes photosensitizers to produce a certain amount of reactive oxygen species (ROS) under light irradiation at an appropriate power to induce manifest and irreversible damage to cancer cells.[18,19] Both PTT and PDT have unique advantages, such as low side effects, high therapeutic selectivity and negligible drug resistance.[20–24] Besides, SDT utilizes sonosensitizers to generate ROS *via* the sonodynamic effect under ultrasound (US) irradiation.[25–27] Similar to PDT, SDT has been reported to have slight toxicity to adjacent normal tissues and thus widely used for tumor ablation.[28–31] In addition, because US penetrates deeply into the tumor tissues, SDT can overcome the tissue penetration depth limitations.[32] However, tumors show a complicated microenvironment that will compromise the efficacies of various therapies.[33] For example, the expression of heat shock proteins limits the PTT effect for ablating tumor cells.[33,34] The hypoxic tumor microenvironment with high levels of glutathione can obviously restrict the efficacies of PDT and SDT.[35,36] Therefore, a sole therapeutic strategy usually fails to achieve satisfactory outcomes, and the combination of multiple therapies is highly desired.[37]

Semiconducting polymer nanoparticles (SPN) formed from semiconducting polymers (SPs) with a π-conjugated aromatic framework have been used for fluorescence imaging, PTT, PDT and SDT due to their good optical absorbance, structural stability and high biosafety.[38] For example, near-infrared (NIR)-absorbing poly[2,6-(4,4-bis-(2-ethylhexyl)-4*H*-cyclopenta[2,1-*b*;3,4*b*′]-dithiophene)-*alt*-4,7(2,1,3-benzothiadiazole)] (PCPDTBT) can be activated by NIR light to produce $^1O_2$ and heat for both PDT and PTT.[39–41] Another SP, poly[2,7-(9,9-di-octyl-fluorene)-*alt*-4,7-bis-(thiophen-2-yl)benzo-2,1,3-thiadiazole] (PFODBT), has been used as a sonosensitizer to mediate SDT *via* generating $^1O_2$.[42–47] Therefore, the integration of two different SPs into one therapeutic system will enable combinational therapy with high efficacy, which however has been poorly reported.

In this study, radioactive hybrid semiconducting polymer nanoparticles (SPN$_H$) are fabricated to enable imaging-guided PDT–PTT–SDT combination therapy for tumor ablation and metastasis inhibition. SPN$_H$ are formed *via* the nano-coprecipitation of PCPDTBT, PFODBT and an amphiphilic triblock copolymer F127 and their surface is labeled with ^{131}I for single photon emission computed tomography (SPECT) imaging (Fig. 1a). Under 808 nm laser and US irradiation, SPN$_H$ mediate the generation of heat by PCPDTBT for PTT, and also abundant $^1O_2$ by PCPDTBT and PFODBT for PDT and SDT. Such a tri-modal therapy can greatly ablate tumor cells to inhibit tumor growth and effectively suppress tumor metastasis in the lungs and liver (Fig. 1b). The therapeutic efficacy of PDT, PTT and SDT combinational

therapy is higher than that of sole SDT and combinational PDT–PTT.

Experimental section

Materials

PCPDTBT and PFODBT were obtained from Sigma-Aldrich (USA). The cell counting kit-8 (CCK-8) was obtained from Molecular Probes Inc. Chemical reagents used in all experiments were provided by Sinopharm (China). 2′,7′-Dichloro-dihydrofluorescein diacetate (H_2DCFDA) and Pluronic® F-127 were purchased from Shanghai Macklin Biochemical Technology Co., Ltd (China). A singlet oxygen sensor green (SOSG) fluorescent probe was obtained from Thermo Fisher Scientific (USA).

Characterization

Morphological characteristics were analyzed using a Tecnai transmission electron microscope (JEOL, TEM JEM-2100, Japan). An IVIS Lumina Series III system was used to obtain the fluorescence images of living animals (IVIS machine, PerkinElmer, USA). An inverted fluorescence microscope (Leica, DMi8, Germany) was used to obtain cell fluorescence images. An absorption spectrophotometer (Persee, TU-1810, Beijing, China) was utilized to detect ultraviolet absorption characteristics. The fluorescence properties were evaluated using a fluorescence spectrophotometer (SHIMADZU, RF-6000, Kyoto, Japan). A zeta potential and particle sizer (Malvern, Zetasizer Nano S90, UK) was used to measure the hydrodynamic sizes and zeta potential values.

Synthesis of SPN$_H$

SPN were synthesized by a nano-precipitation method.[47–49] In general, 0.25 mg of PCPDTBT and 0.25 mg of PFODBT were dissolved in 2 mL of tetrahydrofuran (THF), respectively. 50 mg of Pluronic® F-127 dissolved in 2 mL of THF was blended with the above solution. Then the solution was added into 10 mL of THF/water ($V/V = 1:9$) and sonicated. THF was evaporated overnight, and the solution was filtered through a 200 nm membrane and ultrafiltrated to obtain SPN. SPN$_H$ were obtained by labeling the SPN with ^{131}I. In brief, 1 mg of SPN, 20 mCi Na^{131}I and 1 mg of chloramine-T were mixed and reacted at room temperature for 2 h, and then the solution was centrifuged 5 times to obtain SPN$_H$. A TU-1810 Persee spectrophotometer was used to determine the concentrations of SPN$_H$.

Photothermal effect evaluation

The SPN$_H$ solution was diluted with ultrapure water to prepare samples with SP concentrations of 12.5, 25, 50, and 100 μg mL^{-1}, respectively. An 808 nm laser with a power density of 1.0 W cm^{-2} was used to irradiate the sample solutions for 6 min. A Fotric 220s thermal camera was utilized to record temperature changes every 5 s. After irradiation, the temperatures of SPN$_H$ solutions were measured every 5 s for another 360 s. For the evaluation of the photothermal stability, SPN$_H$ solutions at SP concentrations of 12.5, 25, 50, and 100 μg mL^{-1} were irradiated under the same

6092 | *J. Mater. Chem. B*, 2024, **12**, 6091–6101

This journal is © The Royal Society of Chemistry 2024
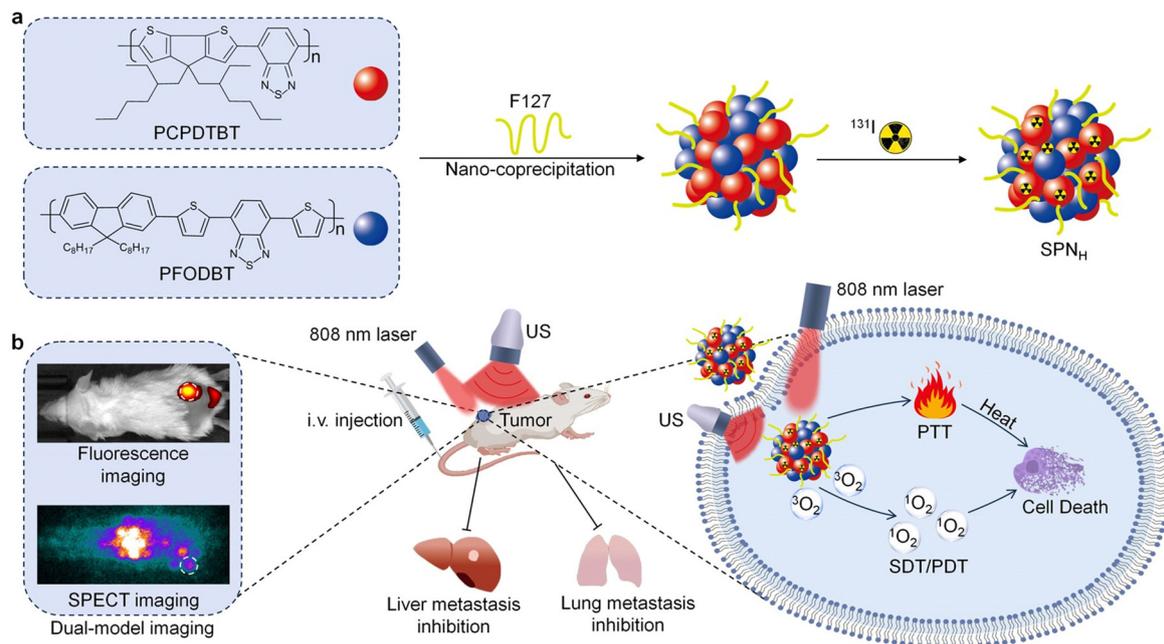
Fig. 1   Design of SPN$_H$ for imaging-guided tri-modal therapy. (a) The chemical structure formulas of PCPDTBT and PFODBT, and the formation of SPN$_H$ *via* nanoprecipitation and labeling of ^{131}I. (b) Schematic illustration of SPN$_H$ for fluorescence/SPECT imaging-guided tri-modal therapy.

conditions, and the changes of temperature were monitored after five laser on and laser off cycles.

Evaluation of $^1O_2$ generation efficacy

A $^1O_2$ fluorescence probe (SOSG) was utilized to measure $^1O_2$ generation efficacy under laser and US irradiation. A SPN$_H$ solution at a SP concentration of 50 μg mL^{-1} (3 mL) was mixed with SOSG (3 μL, 500 μM) and the initial fluorescence intensity (F_0) was measured. The solutions were divided into sole laser (1.0 W cm^{-2}, 10 min), sole US (1.0 W cm^{-2}, 1.0 MHz, 50% cycle, 10 min) and laser (1.0 W cm^{-2}, 5 min) plus US (1.0 W cm^{-2}, 1.0 MHz, 50% cycle, 5 min) groups. The fluorescence intensities of SOSG in solutions (F) after various treatments were recorded. The $^1O_2$ generating efficiency was calculated using F/F_0.

Evaluation of cytotoxicity *in vitro*

4T1 cancer cells were seeded in 96-well cell culture plates and then incubated with SPN$_H$. The cell viability was measured *via* cell counting kit 8 (CCK-8) analysis.

Evaluation of the therapeutic effect *in vitro*

4T1 cells were treated with PBS (control) or SPN$_H$ at a SP concentration of 50 μg mL^{-1} for 12 h. The cells were then treated with US at a power density of 1.0 W cm^{-2} (1.0 MHz, 50% cycle, 2.5 min) and an 808 nm laser at a power density of 1.0 W cm^{-2} (2.5 min). To confirm the PTT effect, the treated cells were also incubated with *N*-acetyl-L-cysteine (NAC) to scavenge ROS.[50–52] During laser irradiation, the temperatures of cells were controlled below 43 °C to verify the PDT effect. After the cells were cultured for another 12 h, the CCK-8 assay was used to measure the cell viability.

In vitro dead/live staining analysis

4T1 cells were incubated with SPN$_H$ at a SP concentration of 50 μg mL^{-1} for 12 h and then treated with US at a power density of 1.0 W cm^{-2} (1.0 MHz, 50% cycle, 2.5 min) and an 808 nm laser at a power density of 1.0 W cm^{-2} (2.5 min). After that, the cells were cultured for 12 h and stained with 0.1% PI and 0.1% Calcein for 15 min, and the dead/live staining images of cells were then obtained.

Detection of ROS in cells

After 4T1 cells were incubated with SPN$_H$ (50 μg mL^{-1}) for 12 h, the fluorescent dye H$_2$DCFDA solution was added into each well for cell incubation. The cells were then treated with US (1.0 W cm^{-2}, 1.0 MHz, 50% cycle, 2.5 min) and an 808 nm laser (1.0 W cm^{-2}, 2.5 min). The generation of ROS in cells was evaluated by detecting fluorescence signals using an inverted fluorescence microscope.

Establishment of mouse tumor models

All the animal experiments were approved by the Animal Care and Use Committee of Donghua University. BALB/c mice (5-week-old) were used to establish subcutaneous 4T1 tumor-bearing mouse models. In brief, 2×10^6 4T1 cells suspended in PBS were injected into the right flank of mice to build the mouse tumor models.

In vivo fluorescence and SPECT imaging

After systemic administration of SPN$_H$ (SP concentration = 250 μg mL^{-1}, 200 μL) into subcutaneous 4T1 tumor-bearing mice, the fluorescence images of mice at predetermined time points were captured using an IVIS Lumina Series III imaging system. After 27 h of systemic administration, the mouse tumor

models were euthanized to extract tumors and main organs for detecting their fluorescence signals.

The *in vivo* SPECT imaging of 4T1 tumor-bearing mice was performed using an Infinia GE SPECT equipped with a Xeleris workstation and a high energy general purpose detector (GE Inc., Fairfield, CT). The mice were intravenously injected with SPN_H at a SP concentration of 250 μg mL^{-1} (200 μL). At different time points post injection, SPECT images of tumor-bearing mice were captured and the signal values of tumor sites were measured. At 27 h post-injection, the main organs and tumors were extracted to measure the SPECT signals.

In vivo PTT effect evaluation

4T1 tumor-bearing BALB/c mice were intravenously injected with PBS or SPN_H (200 μL, 250 μg mL^{-1}). At 12 h after post-injection, the tumor sites of mice were exposed to 808 nm laser irradiation for 300 s (1.0 W cm^{-2}). An infrared thermographic camera (Fotric 225, USA) was used to record the temperature changes in the tumor area during laser irradiation.

In vivo tumor therapy

4T1 tumor-bearing BALB/c mice were intravenously injected with PBS or SPN_H (250 μg mL^{-1}, 200 μL). The mice for *in vivo* therapeutic evaluation were divided into six groups: PBS (control), PBS + laser + US, SPN_H, SPN_H + US, SPN_H + laser, and SPN_H + US + laser (n = 5). The tumors were irradiated by US (1.0 W cm^{-2}, 1.0 MHz, 50% cycle, 5 min) and/or using an 808 nm laser (1.0 W cm^{-2}, 5 min) in different groups. The tumor volumes were calculated based on the measured tumor sizes and the body weights of mice were recorded. After 14 days of treatment, the mice in each group were sacrificed to extract the tumors and main organs for histological analysis *via* hematoxylin and eosin (H&E) staining. The Kaplan–Meier survival curves of mice were established by recording the survival of mice after various treatments.

In vivo metastasis inhibition analysis

4T1 tumor-bearing BALB/c mice were randomly divided into six groups: PBS (control), PBS + laser + US, SPN_H, SPN_H + US, SPN_H + laser and SPN_H + US + laser (n = 5). These mice were injected with PBS or SPN_H (250 μg mL^{-1}, 200 μL) and the tumors were exposed to US (1.0 W cm^{-2}, 1.0 MHz, 50% cycle, 5 min) and 808 nm laser (1.0 W cm^{-2}, 5 min) irradiation at 24 h post-injection. After 30 days of treatment, the treated mice were euthanized to obtain the lungs and livers for H&E staining. The metastasis inhibition efficacies in the lungs and livers were analyzed by calculating the areas of metastatic tumor nodules.

Statistical analysis

All the experiments were repeated at least three times, and mean ± standard deviation (SD) was used to represent the data. The experimental data were statistically analyzed by one-way ANOVA. The values of p less than 0.05 indicated statistical significance, that is, (*)$p < 0.05$, (**)$p < 0.01$, and (***)$p < 0.001$.

Results and discussion

Synthesis and characterization of SPN_H

SPN were synthesized *via* a nanoprecipitation method using two SPs (PCPDTBT and PFODBT) and F127.[47–49] At the optimized feeding weight of PCPDTBT, PFODBT and F127 of 1 : 1 : 200, the hydrodynamic size was the smallest (62.1 nm), while it was larger than 110 nm at other feeding weights (Table S1, ESI†). Then SPN were labeled with ^{131}I to form the final SPN_H. ^{131}I was covalently immobilized onto the aromatic backbone of SPs *via* electrophilic substitution of protons, which enabled stable labeling. The transmission electron microscopy (TEM) image demonstrated that SPN_H displayed a homogeneous granular morphology with a diameter of about 60 nm (Fig. 2a). Subsequently, the hydrodynamic size of SPN_H was measured to be 62.1 nm (Fig. 2b). The zeta potential of SPN_H was −25.7 mV (Fig. 2c), and this negative charge was conducive to *in vivo* stability and biosafety.[53] Furthermore, the average sizes of SPN_H in water, PBS and DMEM cell culture medium did not change significantly (Fig. 2d). Their polydispersity index (PDI) was measured to be around 0.15 and did not obviously change in water, PBS and DMEM cell culture medium within 14 days (Fig. S1, ESI†), demonstrating that they had good stability in different systems. The absorbance and fluorescence properties of SPN_H were detected. SPN_H displayed the definite characteristic peaks of PCPDTBT and PFODBT at 380, 540 and 665 nm. The characteristic absorption peaks of SPN_H at 380 and 665 nm overlapped with those of PCPDTBT, while the characteristic absorption peak at 540 nm was assigned to PFODBT (Fig. 2e). The fluorescence spectrum showed that SPN_H had a fluorescence peak at 845 nm (Fig. 2f). The radiolabeling efficacy of ^{131}I in SPN_H was as high as 99.0% after purification by centrifugation. After 24 h incubation in fetal bovine serum (FBS) and PBS at 37 °C, the radiochemical purity of SPN_H remained higher than 90.8% (Fig. S2, ESI†), which indicated the good radiochemical stability of SPN_H.

The photothermal effect of SPN_H under laser irradiation was evaluated. Thermal imaging showed that the temperatures of solutions containing SPN_H under laser irradiation were positively correlated with SP concentration (Fig. S3, ESI†). The temperature of SPN_H solutions was found to increase to 36.2, 40.6, 47.7 and 59.4 °C for irradiated groups at concentrations of 12.5, 25, 50 and 100 μg mL^{-1}, respectively (Fig. 2g). At concentrations of 12.5, 25, 50, and 100 μg mL^{-1}, the maximum temperatures of SPN_H solutions after five laser on–off cycles did not have obvious changes (Fig. 2h), suggesting the excellent photothermal stability of SPN_H. In the photothermal cycle experiment, the photothermal conversion efficiency of SPN_H was measured to be 31.9% under 808 nm laser irradiation.[54] The photodynamic effect and sonodynamic effect of SPN_H were then evaluated by using singlet oxygen sensor green (SOSG) as a $^1O_2$ probe. The fluorescence intensities of SOSG in the aqueous solution containing SPN_H showed a gradual increase under both laser and US irradiation (Fig. S4, ESI†). After 10 min, the fluorescence intensities of SOSG increased 9.3 times for both laser and US irradiation, which was higher than those in the

6094 | *J. Mater. Chem. B*, 2024, **12**, 6091–6101

This journal is © The Royal Society of Chemistry 2024
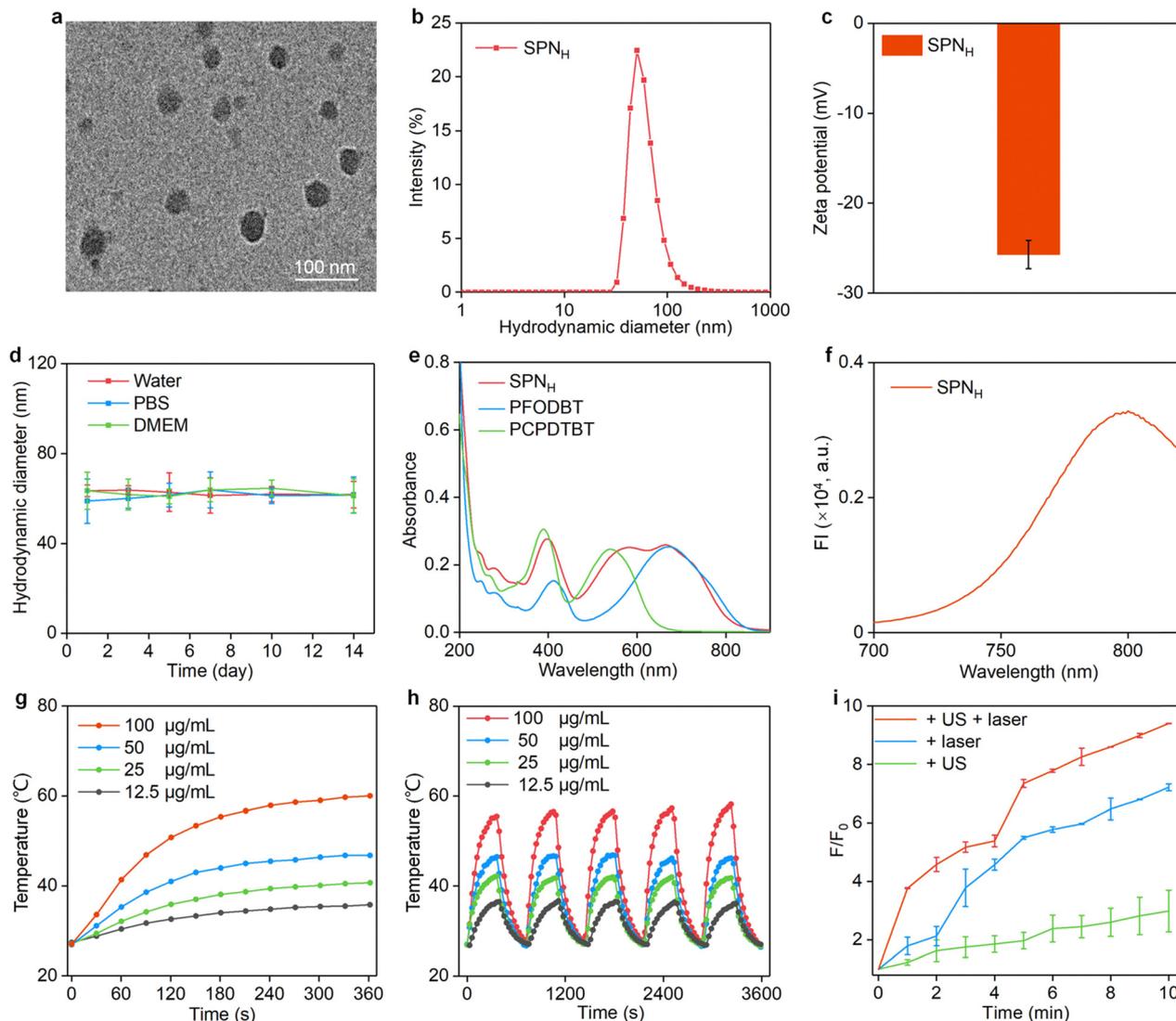
Fig. 2 Characterization of SPN_H. (a) Morphology characterization of SPN_H using TEM imaging. (b) Hydrodynamic diameter profiles of SPN_H measured in aqueous solution. (c) Determination of the zeta potential of SPN_H in aqueous solution ($n = 3$). (d) Hydrodynamic diameters of SPN_H measured in water on days 1, 3, 5, 7, 10 and 14 ($n = 5$). (e) Ultraviolet–visible absorption spectra of PFODBT, PCPDTBT and SPN_H. (f) Fluorescence spectrum of SPN_H. (g) Temperature curves of aqueous solutions containing SPN_H under 808 nm laser irradiation for 360 s. (h) The photothermal stability study of SPN_H after five laser on/off cycles at different concentrations. (i) The $^1O_2$ generation efficacies of SPN_H under US and laser irradiation ($n = 3$).

case of sole US (3.0 times) and laser (7.2 times) irradiation (Fig. 2i). The results illustrated that the amount of $^1O_2$ produced by photodynamic and sonodynamic combinational effects was higher than that of the sole photodynamic effect or sonodynamic effect.

Evaluation of *in vitro* therapeutic efficacy and ROS generation

The *in vitro* cytotoxicity of SPN_H was determined using the CCK-8 assay. 4T1 cells were incubated with SPN_H at various concentrations (0, 6, 12, 25, 50 and 100 μg mL^{-1}) for 24 h, and the results showed that the cell viability remained higher than 90.0% (Fig. 3a), which suggested that SPN_H had low cytotoxicity. The *in vitro* therapeutic efficacy of SPN_H at a concentration of 50 μg mL^{-1} was studied. The viability of 4T1 cells in the SPN_H

+ US + laser group was only 9.6% due to the PDT, PTT and SDT combinational therapy (Fig. 3b). In addition, the 4T1 cell viability in SPN_H + US and SPN_H + laser groups was 68.2% and 38.1%, respectively. In order to distinguish the toxic effects of PDT and PTT in the SPN_H + laser group, NAC was used to eliminate the generation of ROS for only the PTT effect or the temperatures were controlled below 43 °C for the sole PDT effect. Both SPN_H + laser + NAC and SPN_H + laser (<43 °C) groups showed certain therapeutic effects, and the cell viability was 73.4% for the SPN_H + laser + NAC group and 60.8% for the SPN_H + laser (<43 °C) group (Fig. S5, ESI†). These results demonstrated that the cell viability in the SPN_H + US + laser group decreased much more significantly compared to that in SPN_H + US and SPN_H + laser groups, revealing the better *in vitro* therapeutic efficacy of PDT–PTT–SDT combinational therapy.

This journal is © The Royal Society of Chemistry 2024

J. Mater. Chem. B, 2024, **12**, 6091–6101 | **6095**
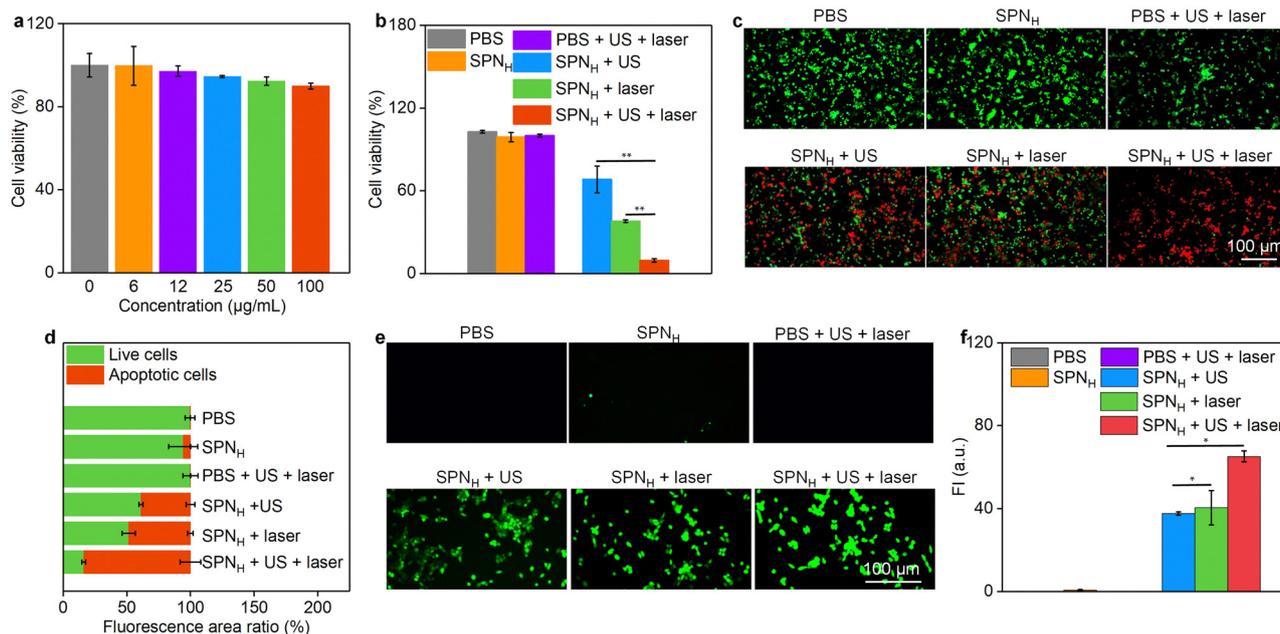
Fig. 3 Evaluation of *in vitro* therapeutic efficacy and ROS generation. (a) Cell viability analysis of 4T1 cells after 24 h incubation with different concentrations of SPN_H (*n* = 5). (b) Cell viability of 4T1 cancer cells in each group. (c) Fluorescence images of stained 4T1 cells to show live/apoptotic cells. (d) Quantitative analysis of live and apoptotic cell ratios after various treatments. (e) Fluorescence images of intracellular ROS generation after various treatments. (f) The mean fluorescence intensities of ROS stained signals in treated 4T1 cells.

The *in vivo* therapeutic efficacy was also verified using Calcein-AM/PI staining to show the live and apoptotic cells.[55] The apoptotic cells were remarkably observed in SPN_H + laser, SPN_H + US and SPN_H + US + laser groups (red fluorescence signals), while nearly no apoptotic cells could be found in the other groups (Fig. 3c). More importantly, the signals of red fluorescence of apoptotic cells in the SPN_H + US + laser group were much stronger compared to those in SPN_H + laser and SPN_H + US groups. Through quantitative analysis of the green/red fluorescence intensity, we found that the proportions of apoptotic cells in the SPN_H + US + laser group were as high as 83.8%, while those were 48.4% and 38.9% in SPN_H + laser and SPN_H + US groups, respectively (Fig. 3d). These results revealed that the SPN_H + US + laser group had the highest efficacy in killing cancer cells.

Intracellular ROS production after different treatments was also detected using H_2DCFDA as the indicator. Conspicuous ROS generation occurred in SPN_H + US + laser, SPN_H + laser, and SPN_H + US groups, while the ROS levels in PBS, SPN_H and PBS + laser + US groups were negligible (Fig. 3e). The quantitative analysis showed that the fluorescence intensity of ROS generation in the SPN_H + US + laser group was approximately 1.5- and 1.6-fold higher than those in SPN_H + laser and SPN_H + US groups, respectively (Fig. 3f). These results confirmed the abundant ROS generation in the SPN_H + US + laser group, which should be due to the SDT and PDT effects.

In vivo fluorescence and SPECT imaging

Mouse models with subcutaneous 4T1 tumors were utilized for evaluating *in vivo* fluorescence and SPECT imaging. After intravenous injection of SPN_H, the fluorescence signals of tumor sites gradually increased and reached the maximum value in 12 h (Fig. 4a). At 12 h post-injection, the fluorescence intensity of tumors was nearly 3000 times higher compared to the initial fluorescence intensity (Fig. 4b). These results suggested the effective diagnosis of 4T1 tumors using fluorescence imaging. In addition, manifest fluorescence signals could be observed in isolated livers and tumors, which were barely detected in the heart, spleen, lungs and kidneys (Fig. 4c). The quantitative data illustrated that the fluorescence intensity of the liver and tumors was much higher than those of the other organs (Fig. 4d).

As for SPECT imaging, the signals in tumor sites could be clearly detected at 2 h post-injection of SPN_H and the signal gradually increased until 12 h (Fig. 4e). The maximum signal value at 12 h post-injection increased by around 2.4-fold compared to the initial value (Fig. 4f). The *ex vivo* SPECT imaging illustrated that SPN_H inclined to accumulate in the liver and tumors because the signals could be observed in the liver and tumors (Fig. S6, ESI†). The signal intensities of the liver and tumors were overall higher than those in the heart, spleen, lungs and kidneys (Fig. 4g). These results illustrated that SPN_H could be used for SPECT imaging of tumors, and the accumulation effect of SPN_H observed *via* fluorescence and SPECT imaging was similar. After intravenous injection, SPN_H exhibited good pharmacokinetic properties as they still could be detected in the bloodstream for 84 h (Fig. S7, ESI†).[56]

In vivo antitumor efficacy evaluation

After treatment, the tumors were used to confirm the ROS production using a fluorescence probe. The ROS signal (green
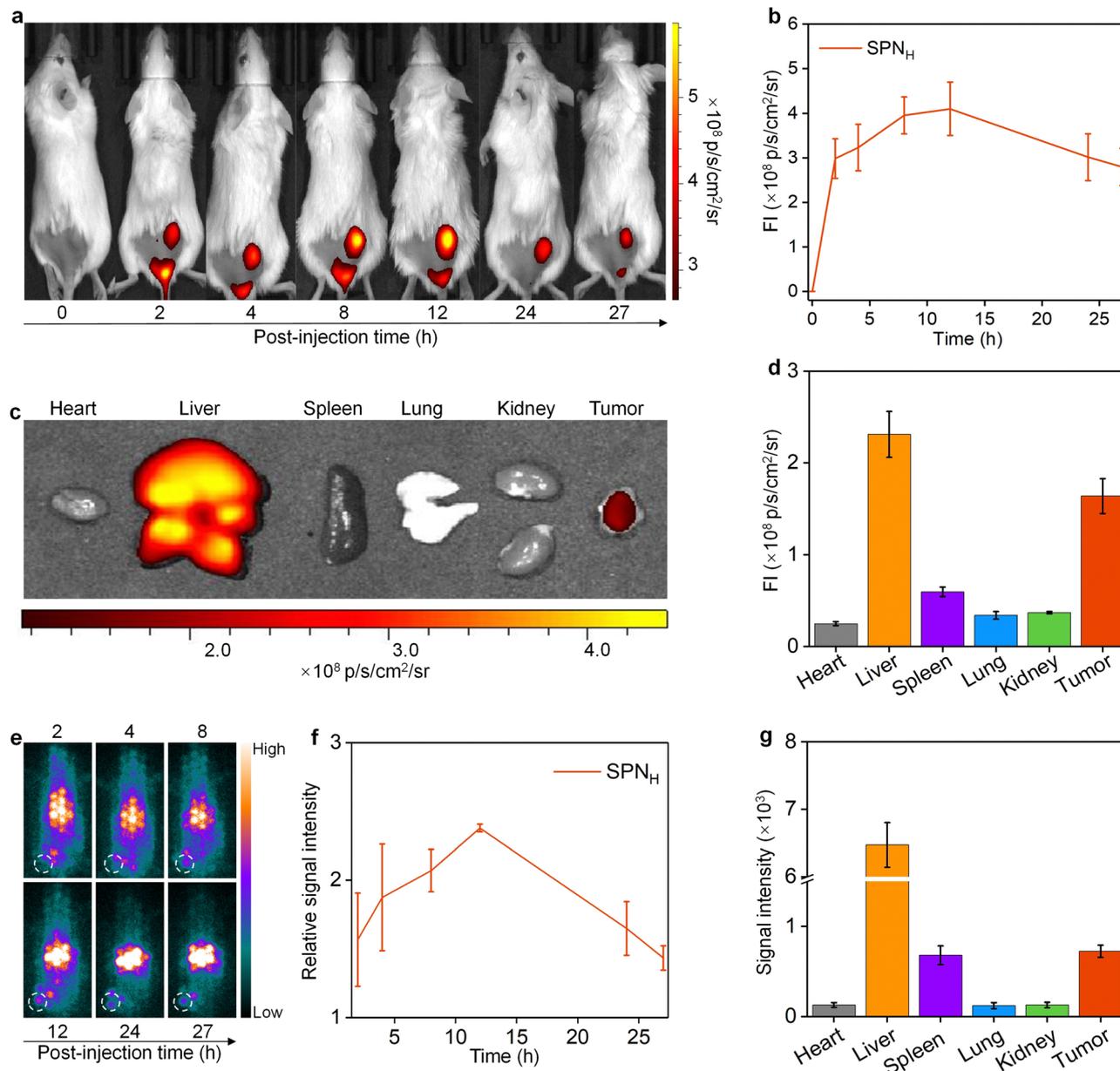
Fig. 4 *In vivo* fluorescence and SPECT imaging. (a) The fluorescence images of tumor-bearing mice at different time points after SPN$_H$ injection through the tail vein. (b) Intensity of fluorescence signals in the tumor areas of mice ($n = 3$). (c) The fluorescence images of the tumors and main organs of mice at 27 h after intravenous injection of SPN$_H$. (d) Quantitative analysis of fluorescence intensity in tumors and major organs ($n = 3$). (e) The SPECT images of 4T1 tumor-bearing mice post intravenous injection of SPN$_H$ (^{131}I, 1 mCi). (f) The quantitative analysis of the relative signal intensity of tumor areas. (g) The quantitative analysis of the signal intensity of major organs and tumors.

fluorescence) was observed only in SPN$_H$ + US, SPN$_H$ + laser, and SPN$_H$ + US + laser groups (Fig. S8, ESI†), confirming the generation of $^1O_2$. Compared with the PBS group, the ROS green fluorescence intensity was increased 7.8, 16.1 and 28.5 times in SPN$_H$ + US, SPN$_H$ + laser, and SPN$_H$ + US + laser groups, respectively.

Because the maximum accumulation of SPN$_H$ at the tumor sites occurred at 12 h post-injection, the tumors were irradiated by a laser and/or US at this time point to enable therapeutic actions. Due to the photothermal effect of PCPDTBT, the *in vivo* PTT effect of SPN$_H$ was investigated.[57,58] Two groups of mice

with 4T1 tumors were randomly assigned to PBS and SPN$_H$ groups. The real-time temperatures of the tumor areas under 808 nm laser irradiation (1.0 W cm^{-2}) were monitored. The tumor temperature in the SPN$_H$ + laser group gradually increased under laser irradiation, while in the PBS + laser group it did not have obvious elevation (Fig. 5a), which verified the *in vivo* PTT effect. The temperature curves of tumor sites illustrated that the temperature in the SPN$_H$ + laser group could obviously increase to 55 °C after 300 s of laser irradiation (Fig. 5b).

The mouse models with 4T1 tumors were used to evaluate the *in vivo* antitumor efficacy of SPN$_H$ by monitoring tumor

This journal is © The Royal Society of Chemistry 2024

J. Mater. Chem. B, 2024, **12**, 6091–6101 | **6097**
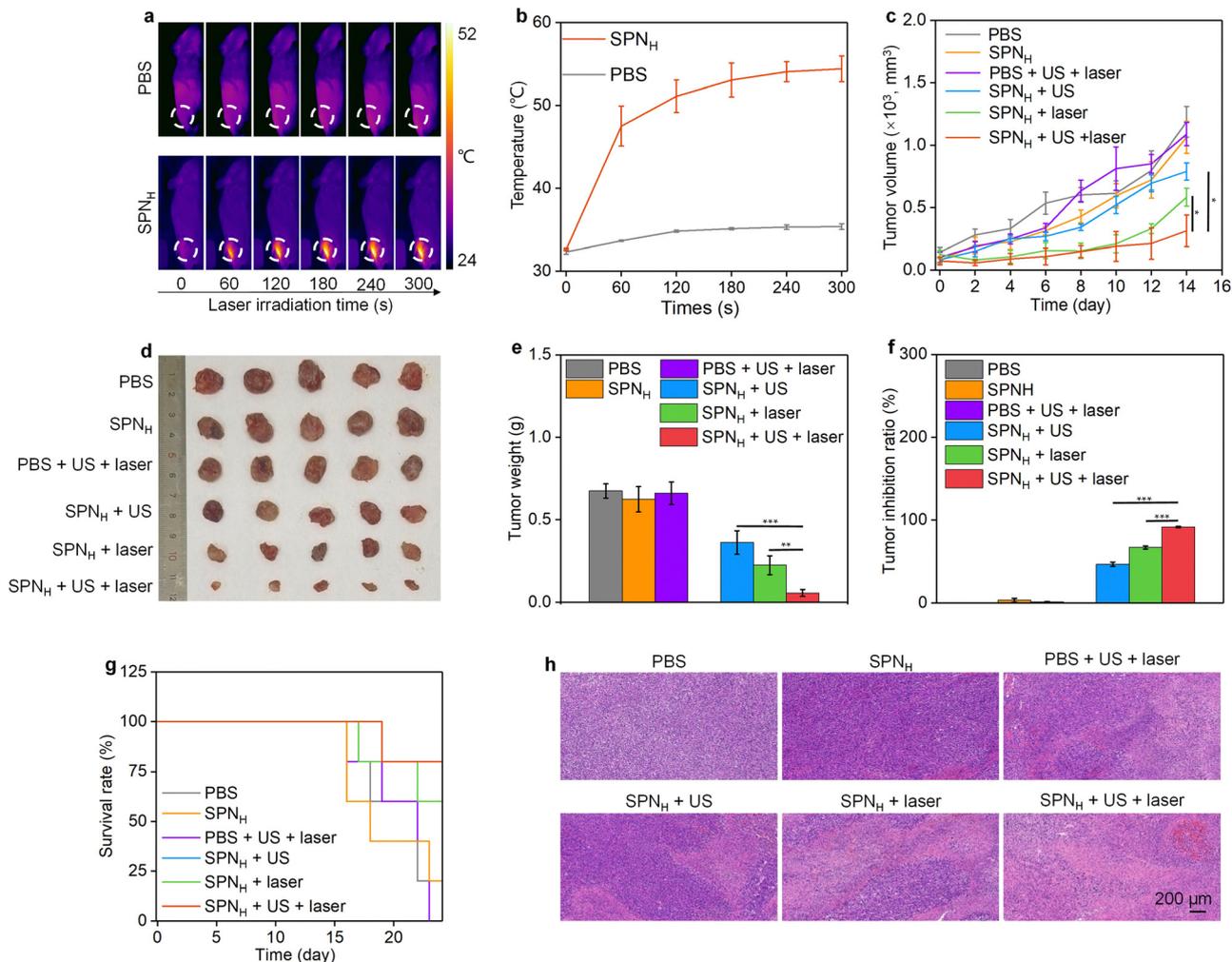
Fig. 5 Evaluation of *in vivo* antitumor efficacy. (a) Thermal imaging of tumor–bearing mice under 808 nm laser irradiation for 300 s (1 W cm^{-2}) at 12 h after systemic administration of PBS or SPN$_H$ (250 μg mL^{-1}, 200 μL). (b) Mean temperatures of tumors at 0, 60, 120, 180, 240 and 300 s under 808 nm laser irradiation (n = 3). (c) Tumor volumes from the six groups after injection of PBS or SPN$_H$ at a concentration of 250 μg mL^{-1} (200 μL) without or with US, laser and US plus laser irradiation (n = 5). (d) The tumor photographs from mice in various treatment groups (n = 5). (e) The tumor weights in various treatment groups (n = 5). (f) The tumor inhibition efficacy in various treatment groups (n = 5). (g) Survival curves of mice after treatment (n = 5). (h) H&E staining images of tumors in various treatment groups.

volumes and measuring tumor weights.[59,60] After 14 days of observation, the tumor volumes in the SPN$_H$ + laser + US group were 3.8-, 3.4-, 3.5-, 2.5- and 1.9-fold lower than those in PBS, SPN$_H$, PBS + US + laser, SPN$_H$ + US and SPN$_H$ + laser groups, respectively (Fig. 5c). Tumor photographs showed that the sizes of all five tumors in the SPN$_H$ + laser group were smaller than those in the SPN$_H$ + US group (Fig. 5d). This should be because the nanoparticles mediated both PTT and PDT in the SPN$_H$ + laser group to ablate the tumor cells, while they only enabled SDT in the SPN$_H$ + US group. In the SPN$_H$ + US + laser group, all five tumors showed the smallest sizes. Additionally, the mean tumor weight in the SPN$_H$ + US + laser group was only 0.06 g, which was 6.3- and 3.9-fold lower compared to those in the SPN$_H$ + US and SPN$_H$ + laser groups, respectively (Fig. 5e). Tumors in the SPN$_H$ + US + laser group showed a conspicuous tumor inhibition rate (91.5%), which was higher than those in SPN$_H$ + US (46.4%) and SPN$_H$ + laser (66.7%) groups (Fig. 5f).

These results verified the highest *in vivo* antitumor efficacy in the SPN$_H$ + US + laser group *via* the PDT–PTT–SDT combinational effect.

Next, the mouse survival rates were recorded for 24 days after different treatments. All mice in PBS and PBS + US + laser groups died, while the survival rate of mice in the SPN$_H$ + US + laser group remained 80% (Fig. 5g). The H&E staining results further indicated that tumor cell necrosis/apoptosis could be observed in SPN$_H$ + US, SPN$_H$ + laser and SPN$_H$ + US + laser groups, but the tumors in the SPN$_H$ + US + laser group displayed the most manifest cell necrosis/apoptosis (Fig. 5h).

Evaluation of the antimetastatic effect

The metastasis inhibition of breast cancer is pivotal to ensure ideal therapeutic effects.[61–63] The *in vivo* antimetastatic effect of SPN$_H$ was evaluated using H&E staining after treatment for 22 days. The combinational therapy in the SPN$_H$ + US + laser

6098 | *J. Mater. Chem. B*, 2024, **12**, 6091–6101

This journal is © The Royal Society of Chemistry 2024
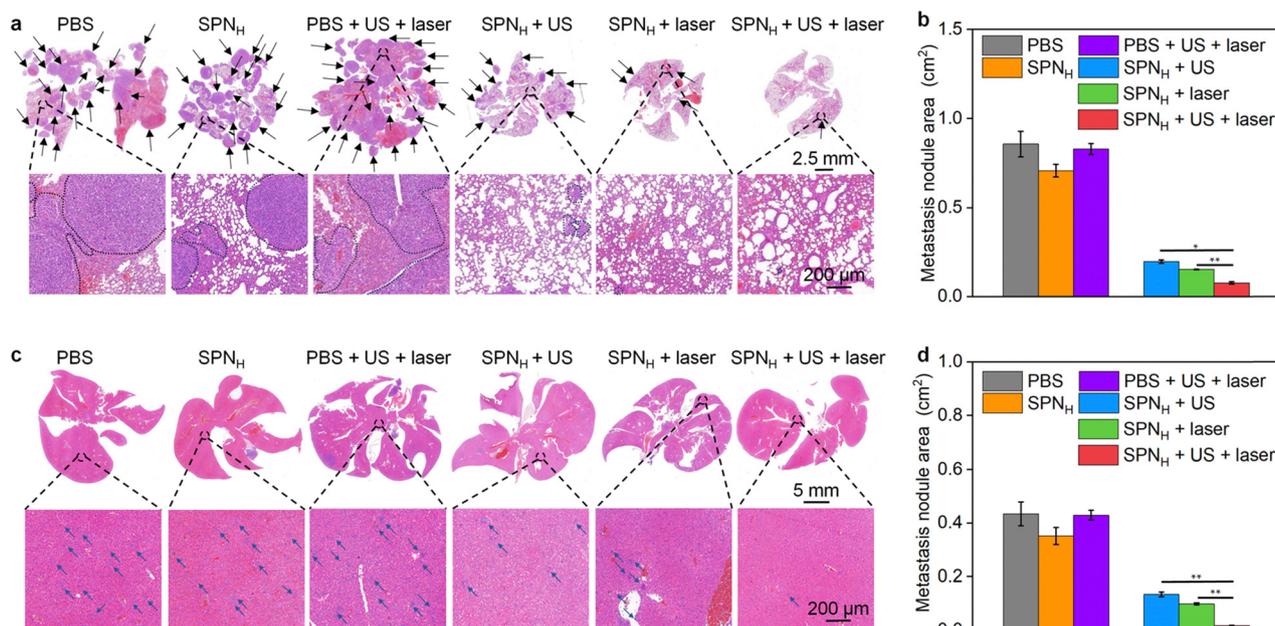
Fig. 6 Evaluation of the *in vivo* antimetastatic effect. (a) Representative H&E staining images of the lungs for various groups (the black arrow shows the location of the metastasis tumor nodules; the black dotted line represents the metastasis tumor nodules). (b) The areas of metastasis tumor nodules in isolated lung tissues in various groups ($n = 5$). (c) H&E staining images of the livers after treatment (blue arrows indicate the location of metastasis tumor nodules). (d) The areas of tumor metastasis nodules in the liver tissues of various groups ($n = 5$).

group conspicuously suppressed tumor metastasis in the lungs because nearly no tumor nodules were observed in H&E staining images (Fig. 6a). However, the tumor nodules could be found in all other groups. The areas of metastatic nodules in the lung tissues were 0.43, 0.35 and 0.43 cm^2 for PBS, SPN$_H$ and PBS + US + laser groups, respectively, while the area of metastatic nodules was only 0.02 cm^2 for the SPN$_H$ + US + laser group (Fig. 6b). Obvious metastatic tumor nodules were also found in the liver tissues of PBS, SPN$_H$ and PBS + US + laser groups, while very small numbers of tumor nodules could be observed in the SPN$_H$ + US + laser group (Fig. 6c). The area of liver metastatic tumor nodules for the SPN$_H$ + US + laser group was as low as 0.08 cm^2 (Fig. 6d). These results revealed that the treatment in the SPN$_H$ + US + laser group could remarkably restrain metastases in lung and liver tissues with the highest antimetastatic effect.

After various treatments, there were no manifest changes in the body weights of mice (Fig. S9, ESI†). As observed in the H&E staining images, the other isolated organs (heart, spleen and kidneys) in the SPN$_H$ + US + laser group showed normality that was consistent with those in the PBS group (Fig. S10, ESI†). These results verified the good biosafety of SPN$_H$ in living subjects.

Conclusions

We herein have designed radioactive hybrid semiconducting polymer nanoparticles (SPN$_H$) for imaging-guided tri-modal therapy of breast cancer. SPN$_H$ containing two semiconducting polymers and labeled ^{131}I showed good radiolabeling stability and photodynamic, photothermal and sonodynamic effects, allowing for fluorescence and SPECT imaging and combinational therapy. The formed SPN$_H$ had a small size of around 60 nm, enabling their effective accumulation in subcutaneous 4T1 tumors. Through *in vivo* fluorescence and SPECT imaging, subcutaneous 4T1 tumors could be clearly diagnosed after injection of SPN$_H$. Under laser and US irradiation, SPN$_H$ mediated the PDT–PTT–SDT combination effect by generating ROS and heat, which enabled a much better antitumor efficacy in inhibiting tumor growth and metastasis compared to sole SDT and combinational PDT–PTT. In consideration of the simple preparation processes, other antitumor drugs can be integrated into SPN$_H$ to further improve the antitumor efficacy. Thus, this research can provide a theranostic nanomedicine for imaging-guided effective treatment of tumors.

Author contributions

J. Gu, D. Cheng and H. Li performed all experimental works and data analyses and wrote the original draft. T. Yu, Z. Zhang and Y. Liu analysed the data. X. Wang, X. Lu and J. Li supervised the project and revised the manuscript.

Conflicts of interest

The authors declare no conflicts of interest.

Acknowledgements

References

1 S. Wang, K. Li, Y. Chen, H. Chen, M. Ma, J. Feng, Q. Zhao and J. Shi, *Biomaterials*, 2015, **39**, 206–217.

2 X. Sun, P. K. Chintakunta, A. A. Badachhape, R. Bhavane, H.-J. Lee, D. S. Yang, Z. Starosolski, K. B. Ghaghada, P. G. Vekilov, A. V. Annapragada and E. A. Tanifum, *Adv. Sci.*, 2023, **10**, 2206435.

3 G. Song, C. Ji, C. Liang, X. Song, X. Yi, Z. Dong, K. Yang and Z. Liu, *Biomaterials*, 2017, **112**, 257–263.

4 D. Wang, T. Nie, C. Huang, Z. Chen, X. Ma, W. Fang, Y. Huang, L. Luo and Z. Xiao, *Small*, 2022, **18**, 2203227.

5 L. Ge, C. Qiao, Y. Tang, X. Zhang and X. Jiang, *Nano Lett.*, 2021, **21**, 3218–3224.

6 I. Kola and J. Landis, *Nat. Rev. Drug Discov.*, 2004, **3**, 711–716.

7 S. Gao, T. Li, Y. Guo, C. Sun, B. Xianyu and H. Xu, *Adv. Mater.*, 2020, **32**, 1907568.

8 N. Ogrinc, P. Saudemont, Z. Takats, M. Salzet and I. Fournier, *Trends Mol. Med.*, 2021, **27**, 602–615.

9 X. Guan, L. Sun, Y. Shen, F. Jin, X. Bo, C. Zhu, X. Han, X. Li, Y. Chen, H. Xu and W. Yue, *Nat. Commun.*, 2022, **13**, 2834.

10 C. Jian, T. Wu, L. Wang, C. Gao, Z. Fu, Q. Zhang and C. Shi, *Small*, 2024, 2309279.

11 S. Fu, Y. Li, L. Shen, Y. Chen, J. Lu, Y. Ran, Y. Zhao, H. Tang, L. Tan, Q. Lin and Y. Hao, *Small*, 2024, 2309537.

12 T. Liu, X. Si, L. Liu, S. Ma, Z. Huang, Y. Zhang, W. Song, Y. Zhang and X. Chen, *ACS Nano*, 2024, **18**, 3087–3100.

13 S. S. Lucky, Y. Soo Kc, F. Zhang and Y. Zhang, *Chem. Rev.*, 2015, **115**, 1990–2042.

14 S. Geng, P. Guo, J. Wang, Y. Zhang, Y. Shi, X. Li, M. Cao, Y. Song, H. Zhang, Z. Zhang, K. Zhang, H. Song, J. Shi and J. Liu, *Adv. Mater.*, 2024, 2307923.

15 F. Liu, C. Guo, X. Li, Y. Li, S. Xu, T. D. James and L. Wang, *Nano Today*, 2024, **54**, 102116.

16 D. Cheng, J. Gong, P. Wang, J. Zhu, N. Yu, J. Zhao, Q. Zhang and J. Li, *J. Mater. Chem. B*, 2021, **9**, 9316–9323.

17 M. Santha Moorthy, G. Hoang, B. Subramanian, N. Q. Bui, M. Panchanathan, S. Mondal, V. P. Thi Tuong, H. Kim and J. Oh, *J. Mater. Chem. B*, 2018, **6**, 5220–5233.

18 Y. Wang, F. Zhang, H. Lin and F. Qu, *ACS Appl. Mater.*, 2019, **11**, 43964–43975.

19 X. Zhang, J. Cui, J. Liu, X. Chen, M. Chen and J. Wang, *J. Mater. Chem. B*, 2023, **11**, 9516–9524.

20 R. R. Allison, G. H. Downie, R. Cuenca, X.-H. Hu, C. J. H. Childs and C. H. Sibata, *Photodiagn. Photodyn. Ther.*, 2004, **1**, 27–42.

21 Y. Yang, Z. Zeng, E. Almatrafi, D. Huang, C. Zhang, W. Xiong, M. Cheng, C. Zhou, W. Wang, B. Song, X. Tang, G. Zeng, R. Xiao and Z. Li, *Coord. Chem. Rev.*, 2022, **458**, 214427.

22 H. Yang, R. Liu, Y. Xu, L. Qian and Z. Dai, *Nano-Micro Lett.*, 2021, **13**, 35.

23 X.-X. Lu, C. Xue, J.-H. Dong, Y.-Z. Zhang and F. Gao, *J. Mater. Chem. B*, 2024, **12**, 3209–3225.

24 M. Shi, X. Liu, W. Pan, N. Li and B. Tang, *J. Mater. Chem. B*, 2023, **11**, 6478–6490.

25 X. Wang, X. Wang, Q. Yue, H. Xu, X. Zhong, L. Sun, G. Li, Y. Gong, N. Yang, Z. Wang, Z. Liu and L. Cheng, *Nano Today*, 2021, **39**, 101170.

26 B. Liu, F. Du, Z. Feng, X. Xiang, R. Guo, L. Ma, B. Zhu and L. Qiu, *J. Mater. Chem. B*, 2024, **12**, 3636–3658.

27 F. Wang, Y. Fan, Y. Liu, X. Lou, L. Sutrisno, S. Peng and J. Li, *Exploration*, 2024, 20230100.

28 Y. Liu, Y. Wang, W. Zhen, Y. Wang, S. Zhang, Y. Zhao, S. Song, Z. Wu and H. Zhang, *Biomaterials*, 2020, **251**, 120075.

29 S. Li, F. Yang, Y. Wang, L. Jia and X. Hou, *Mater. Horiz.*, 2023, **10**, 5734–5752.

30 Y. Jiang, X. Zhao, J. Huang, J. Li, P. K. Upputuri, H. Sun, X. Han, M. Pramanik, Y. Miao, H. Duan, K. Pu and R. Zhang, *Nat. Commun.*, 2020, **11**, 1857.

31 Z. Xiao, Q. Chen, Y. Yang, S. Tu, B. Wang, Y. Qiu, Y. Jiang, Q. Huang and K. Ai, *Chem. Eng. J.*, 2022, **449**, 137889.

32 F. Gong, L. Cheng, N. Yang, O. Betzer, L. Feng, Q. Zhou, Y. Li, R. Chen, R. Popovtzer and Z. Liu, *Adv. Mater.*, 2019, **31**, 1900730.

33 X. Zhang, L. An, Q. Tian, J. Lin and S. Yang, *J. Mater. Chem. B*, 2020, **8**, 4738–4747.

34 Q. Sun, F. Liu, Z. Wen, J. Xia, H. Li, Y. Xu and S. Sun, *J. Mater. Chem. B*, 2022, **10**, 1369–1377.

35 L. Lei, W. Dai, J. Man, H. Hu, Q. Jin, B. Zhang and Z. Tang, *J. Nanobiotechnol.*, 2023, **21**, 482.

36 M.-M. Pan, P. Li, Y.-P. Yu, M. Jiang, X. Yang, P. Zhang, J. Nie, J. Hu, X. Yu and L. Xu, *Adv. Healthcare Mater.*, 2023, **12**, 2300821.

37 Y. Wang, G. Song, S. Liao, Q. Qin, Y. Zhao, L. Shi, K. Guan, X. Gong, P. Wang, X. Yin, Q. Chen and X.-B. Zhang, *Angew. Chem., Int. Ed.*, 2021, **60**, 19779–19789.

38 P. R. Neumann, F. Erdmann, J. Holthof, G. Hädrich, M. Green, J. Rao and L. A. Dailey, *Adv. Healthcare Mater.*, 2021, **10**, 2001089.

39 J. Feng, C. Zhu, H. Yuan, S. Liu, F. Lv and S. Wang, *Chem. Soc. Rev.*, 2013, **42**, 6620.

40 C. Qian, J. Yu, Y. Chen, Q. Hu, X. Xiao, W. Sun, C. Wang, P. Feng, Q.-D. Shen and Z. Gu, *Adv. Mater.*, 2016, **28**, 3313–3320.

41 N. Yu, M. Ding, F. Wang, J. Zhou, X. Shi, R. Cai and J. Li, *Nano Today*, 2022, **46**, 101600.

42 Y. Pan, J. Li, X. Wang, Y. Sun, J. Li, B. Wang and K. Zhang, *Adv. Funct. Mater.*, 2022, **32**, 2110207.

43 Q. Miao, C. Xie, X. Zhen, Y. Lyu, H. Duan, X. Liu, J. V. Jokerst and K. Pu, *Nat. Biotechnol.*, 2017, **35**, 1102–1110.

6100 | *J. Mater. Chem. B*, 2024, **12**, 6091–6101

This journal is © The Royal Society of Chemistry 2024

44 S. Liao, Y. Wang, Z. Li, Y. Zhang, X. Yin, S. Huan, X.-B. Zhang, S. Liu and G. Song, *Theranostics*, 2022, **12**, 6883–6897.

45 M. Ding, Y. Zhang, N. Yu, J. Zhou, L. Zhu, X. Wang and J. Li, *Adv. Mater.*, 2023, **35**, 2302508.

46 W. Chen, Y. Zhang, Q. Li, Y. Jiang, H. Zhou, Y. Liu, Q. Miao and M. Gao, *J. Am. Chem. Soc.*, 2022, **144**, 6719–6726.

47 N. Yu, M. Li, Y. Zhang, F. Wang, X. Yu, R. Cai and J. Li, *Nano Today*, 2023, **52**, 101944.

48 D. Cheng, J. He, C. Zhang, Y. Zhang, N. Yu, R. Cai, X. Wang and J. Li, *ACS Appl. Nano Mater.*, 2023, **6**, 421–430.

49 X. Chen, D. Cheng, N. Yu, J. Feng, J. Li and L. Lin, *J. Mater. Chem. B*, 2024, **12**, 1296–1306.

50 L. S. Gomez-Aparicio, J. Bernáldez-Sarabia, T. A. Camacho-Villegas, P. H. Lugo-Fabres, N. E. Díaz-Martínez, E. Padilla-Camberos, A. Licea-Navarro and A. B. Castro-Ceseña, *Biomater. Sci.*, 2021, **9**, 726–744.

51 H. Huang, C. Dong, M. Chang, L. Ding, L. Chen, W. Feng and Y. Chen, *Exploration*, 2021, **1**, 50–60.

52 J. Wang, M. Liu, X. Zhang, X. Wang, M. Xiong and D. Luo, *Exploration*, 2024, 20230027.

53 P. Ge, B. Niu, Y. Wu, W. Xu, M. Li, H. Sun, H. Zhou, X. Zhang and J. Xie, *Chem. Eng. J*, 2020, **383**, 123228.

54 Y. Lyu, C. Xie, S. A. Chechetka, E. Miyako and K. Pu, *J. Am. Chem. Soc.*, 2016, **138**, 9049–9052.

55 X. Zhen, N. K. Pandey, E. Amador, W. Hu, B. Liu, W. Nong, W. Chen and L. Huang, *Mater. Today Phys.*, 2022, **27**, 100838.

56 Y. Li, J. Lin, Y. He, K. Wang, C. Huang, R. Zhang and X. Liu, *Exploration*, 2024, **4**, 20230054.

57 Z. Liu, C. Hong, C. Pan, Y. Sun, Y. Lv, Y. Wei, X. Wang, W. Zang, Q. Mao, X. Deng, P. Wang, W. Zhu, T. Chen, M. Wu, J. Li and A. Wu, *ACS Mater. Lett.*, 2024, 1593–1605.

58 T. F. Abelha, P. R. Neumann, J. Holthof, C. A. Dreiss, C. Alexander, M. Green and L. A. Dailey, *J. Mater. Chem. B*, 2019, **7**, 5115–5124.

59 C. Song, X. Wu, J. Wang, R. Liu and Y. Zhao, *Nano Today*, 2023, **51**, 101913.

60 Z. Wu, H. Chen, H. Zhang, L. Ye, J. Ke, Y. Liu, P. Sun and M. Hong, *Nano Today*, 2024, **55**, 102214.

61 H. Hu, J. Zhao, K. Ma, J. Wang, X. Wang, T. Mao, C. Xiang, H. Luo, Y. Cheng, M. Yu, Y. Qin, K. Yang, Q. Li, Y. Sun and S. Wang, *J. Controlled Release*, 2023, **359**, 188–205.

62 W. Zeng, Y. Xu, W. Yang, K. Liu, K. Bian and B. Zhang, *Adv. Healthcare Mater.*, 2020, **9**, 2000560.

63 L. Li, M. Zhen, H. Wang, Z. Sun, X. Cao, J. Li, S. Liu, Z. Zhao, C. Zhou, C. Wang and C. Bai, *Nano Today*, 2023, **48**, 101702.

This journal is © The Royal Society of Chemistry 2024

J. Mater. Chem. B, 2024, **12**, 6091–6101 | **6101**